

# The Star Formation Histories of Four Fields Spanning the Minor Axis of NGC 6822<sup>1</sup>

Ted K. Wyder

*California Institute of Technology, 1200 E California Blvd, MC 405-47, Pasadena, CA 91125*

wyder@srl.caltech.edu

## ABSTRACT

The star formation histories of four fields within the Local Group dwarf irregular galaxy NGC 6822 are presented. Each of the fields was imaged by the WFPC2 aboard the *Hubble Space Telescope* and were used to obtain *VI* color-magnitude diagrams for each field reaching  $V \simeq 26$ . The magnitude of the tip of the red giant branch and the red clump were used to determine distances to NGC 6822 that are consistent with previous ground-based measurements. The distance, extinction and star formation history were also determined by fitting the entire color-magnitude diagram in each field. The distances from these fits are consistent with the other determinations within the estimated errors once the systematic effects of uncertainties in the age-metallicity relation are taken into account. The extinction varies among the four fields from approximately the foreground Galactic value to  $\approx 0.4$  mag higher in  $V$  and roughly correlates with the  $60\mu\text{m}$  surface brightness. The star formation histories in the four fields are similar for ages  $\gtrsim 1$  Gyr and are relatively constant or somewhat increasing with time. These old star formation rates are comparable to that expected from the typical gas surface densities at these galactocentric radii and suggest that no large scale redistribution of gas or stars is required to account for the inferred star formation rates. Three of the fields show a drop of a factor of  $\sim 2 - 4$  in the star formation rate about 600 Myr ago while the remaining field centered on the bar shows an increase.

*Subject headings:* galaxies: evolution – galaxies: individual (NGC 6822) – galaxies: irregular – galaxies: stellar content

## 1. Introduction

Much progress has been made in understanding the evolution of galaxies both from comparing the integrated properties of galaxies at various redshifts and from detailed observations of indi-

---

<sup>1</sup>Based on observations made with the NASA/ESA *Hubble Space Telescope*, obtained at the Space Telescope Science Institute, which is operated by the Association of Universities for Research in Astronomy, Inc., under NASA contract NAS 5-26555. These observations are associated with proposal 8314.

vidual nearby galaxies. In particular, the dwarf galaxies in the Local Group provide a unique opportunity to study the evolution of individual systems. Due to their close distances, detailed information about their star formation histories (SFHs) can be derived from the color-magnitude diagrams of their resolved stellar populations. With the exceptions of the Magellanic Clouds, the satellite galaxies of the two most massive galaxies in the Local Group, M31 and the Milky Way, are predominantly dwarf spheroidals and dwarf ellipticals which have little current star formation and whose evolution has presumably been influenced by their proximity to a more massive galaxy. The remaining relatively isolated galaxies in the Local Group are predominantly gas-rich dwarf irregular (dIrr) galaxies which give us the opportunity to study the evolution of isolated galaxies.

The available evidence indicates that no two dIrrs share the exact same SFH although nearly all of them show evidence for a significant population of intermediate and old stars (ages  $> 1$  Gyr) in addition to their ongoing star formation. Furthermore, for many dIrrs such as WLM (Minniti & Zijlstra 1997), Phoenix (Martínez-Delgado et al. 1999) and Leo A (Dolphin et al. 2002), the young blue stars are concentrated in the central regions while the outer regions contain a predominately older, redder stellar population.

NGC 6822 in particular is a Local Group dIrr whose structure fits the patterns described above for dIrrs. This galaxy consists of a bar oriented roughly North-South that contains most of the current sites of star formation which is surrounded by a lower surface brightness area containing a higher proportion of redder, fainter stars (Hodge 1977; Hodge et al. 1991). Based upon wide-field *BRI* images from the 8m Subaru Telescope reaching down to a level of  $M_B \approx 0$ , Komiyama (2002) found that the red stars are distributed symmetrically about the center of the galaxy. While the brightest blue stars are concentrated in the central bar, main sequence stars were detected in the bar and in two arms on either side stretching  $\sim 40'$  from the South-East to the North-West. The blue star distribution follows fairly closely the distribution of HI gas (de Blok & Walter 2000; Weldrake et al. 2002).

The SFH of NGC 6822 has been investigated most recently by Gallart et al. (1996a, b) from ground-based data and by Wyder (2001) from *HST* data. Both studies found that the observed CMDs are best fit with star formation beginning 12–15 Gyr ago although younger ages are allowed if a high initial metallicity is assumed. Based upon their data covering the central  $11.2' \times 10.4'$  area of NGC 6822, Gallart et al. (1996b) found evidence for an increase in the star formation rate (SFR) 100 – 200 Myr ago over the entire area surveyed with the largest increases seen at the ends of the bar. Hodge (1980) found a similar peak in the cluster age distribution 75 – 100 Myr ago. In Wyder (2001), the SFH of NGC 6822 was analyzed in three fields lying in the bar and two other fields sampling more of the outer regions. The overall shapes of SFHs among the five fields were similar and showed a more or less constant or perhaps somewhat increasing SFR with time. However, for ages less than about 600 Myr there were significant variations, implying that stars formed within this time are not yet very well mixed throughout the galaxy. As in the ground-based studies, the bar fields showed an increase in the recent SFR while the SFR decreased in the outer regions.

This paper further explores the SFH of NGC 6822 begun in Wyder (2001) based upon CMDs of four fields that span the minor axis of the bar of NGC 6822, one of which was included in Wyder (2001). The main goal of this work is to generate a SFH profile of the minor axis of NGC 6822 in order to compare the differences between the SFH of the bar with the outer regions. It remains unclear whether the stars have always formed in the central regions and then migrated outwards or whether the stars we observe today in the outer regions were actually formed there as well. A first step in trying to understand the origin of these stellar populations differences is to understand the differences in the ratio of young to old stars between the central and outer regions. A comparison of the star formation rate as a function of time in different regions within each galaxy with the distribution of atomic and molecular gas will provide additional clues to the evolution of these systems.

This paper is organized as follows. §2 presents the data and photometry while §3 briefly summarizes the analysis methods used to extract information about the SFH from the data. The results are presented in §4.

## 2. Observations and Photometry

The data presented here consist of images taken with the WFPC2 aboard *HST* through the *F555W* and *F814W* filters, approximately corresponding to the ground-based *V* and *I* filters, respectively. In each field the PC chip was centered on one of the open clusters C1, C12, C18 and C25 from the list in Hodge (1977) and these field centers were selected to span the bar’s minor axis. The locations of these four fields are shown on an Digitized Sky Survey image of NGC 6822 in Figure 1. Two exposures per filter at each pointing were obtained in order to facilitate the removal of cosmic rays. A list of the files analyzed in this paper is shown in Table 1. The data on the C25 field were included in the data presented previously in Wyder (2001). The clusters appearing in each of these fields have been analyzed by Seth & Hodge (2003).

I obtained photometry for the stars in these images using version 1.1 of the PSF-fitting software package HSTPHOT (Dolphin 2000) which I obtained from the author’s web site.<sup>2</sup> Following the prescription described in more detail in Dolphin (2000) and the HSTPHOT manual, bad pixels in each image were masked out and the two images per filter of each field were added together while at the same time detecting and masking out pixels likely affected by cosmic rays. HSTPHOT was run on the data presented here in a nearly identical manner to the analysis described in Wyder (2001) and the reader is referred to that paper for a more detailed description of the analysis as well as a more detailed discussion of the photometric errors and completeness. The only difference here is that a stricter  $\chi$  limit of  $\chi < 2.5$  was imposed. HSTPHOT automatically determines an aperture correction for each field and chip by comparing the PSF-fit magnitudes with magnitudes

---

<sup>2</sup><http://www.noao.edu/staff/dolphin/hstphot/>

measured within a  $0.05''$  radius aperture. The standard deviations of the aperture corrections are  $\approx 0.05$  magnitudes and represent the dominant source of error in the photometry zeropoint. As in Wyder (2001), artificial star tests were conducted for each of the fields and the results were used to describe the photometric errors and completeness in the analysis presented in the following section. Furthermore, only stars detected on the three WF chips were included in the final photometry list due to the different completeness and errors for stars detected on the PC chip. There are a total of 21,851, 50,004, 47,614, and 37,001 stars detected in the C1, C12, C18 and C25 fields, respectively.

The resulting  $VI$  CMDs for each field are shown in Figure 2 and reach levels of  $V \simeq 26$  for the bluest stars and somewhat fainter for the redder stars. All of the fields contain stars with a wide variety of ages from young main sequence stars a few 10s of Myr old up to red giant branch stars many Gyr old. The relative strength of the main sequence relative to the red clump and red giant branch is higher in the central C12 field compared to the other three fields that sample less of the bar and more of the outer regions. Note also the difference in color of the main sequence which becomes bluer going from the C1 to the C25 field (or equivalently, from West to East across the bar). This changing color of the main sequence is reflected in the varying value of the extinction from the CMD-fitting described in the next section. The most prominent feature in all of the diagrams is the red clump appearing at  $V \approx 25$  and  $1.0 < (V - I) < 1.5$ . Stars in the red clump are core-Helium burning stars with ages of 1 – 10 Gyr and the prominence of the red clump indicates the strength of the intermediate age stellar populations in NGC 6822. As is evident from the CMDs, the magnitude and color of the red clump decrease going from the C1 to the C25 fields which provides additional evidence for variation in dust extinction among the four fields.

### 3. Analysis

In this section I first determine the distance from the CMDs of each of the fields using the tip of the red giant branch (TRGB) and the magnitude of the red clump and then proceed to summarize the methods used to infer the star formation histories from the data. The red clump and TRGB distances provide a useful external check on the distances determined from the fits to the full CMDs.

#### 3.1. Distance from the TRGB magnitude

The TRGB has been shown to be a reliable distance indicator for galaxies with  $[\text{Fe}/\text{H}] < -0.7$  (Lee et al. 1993). The  $I$ -band magnitude distributions for stars with  $1.0 < (V - I) < 2.2$  for each field are plotted in Figure 3 as the solid lines. Following the analysis of Lee et al. (1993), these distributions were convolved with an edge-detecting Sobel Kernel of  $(-2, 0, 2)$  to produce the dotted line in each plot. The position of the first peak in the convolved functions in each panel was used to determine the tip magnitude while the widths of the peaks were used to estimate the

error. The resulting  $I$ -band magnitudes of the RGB tip are listed in Table 2.

I have calculated the TRGB distance for each of the four fields using the prescription described in detail in Lee et al. (1993). This method calculates the distance modulus from the following equation:

$$(m - M)_0 = I_{TRGB} - A_I + BC_I - M_{bol,TRGB} \quad (1)$$

where  $I_{TRGB}$  is the  $I$  magnitude of the TRGB,  $A_I$  the  $I$ -band extinction,  $BC_I$  the bolometric correction and  $M_{bol,TRGB}$  the bolometric magnitude at the TRGB. The extinction for each field was taken from the  $A_V$  values listed in Table 4 and converted to  $A_I$  using the Galactic extinction law. The value of  $BC_I$  for each field was calculated from the  $(V - I)_{TRGB}$ , the color at the TRGB, using the relation

$$BC_I = 0.881 - 0.243(V - I)_{TRGB} \quad (2)$$

determined by Da Costa & Armandroff (1990) from Milky Way globular cluster RGBs. Da Costa & Armandroff (1990) also give  $M_{bol,TRGB}$  as a function of  $[Fe/H]$ :

$$M_{bol,TRGB} = -0.19[Fe/H] - 3.81. \quad (3)$$

Finally, the metallicity was estimated from the relation given in Lee et al. (1993):

$$[Fe/H] = -12.64 + 12.6(V - I)_{-3.5} - 3.3(V - I)_{-3.5}^2 \quad (4)$$

where  $(V - I)_{-3.5}$  is the color of the RGB at  $M_I = -3.5$ , or  $\approx 0.5$  mag below the TRGB. The values of  $(V - I)_{TRGB}$  and  $(V - I)_{-3.5}$  were determined as the median color of RGB stars with  $I$ -band magnitudes within  $\pm 0.1$  mag at the tip or 0.5 mag below. The resulting values of  $(m - M)_0$  are listed in column (5) of Table 2 and are consistent to within the errors with the ground-based TRGB distance modulus of  $(m - M)_0 = 23.4 \pm 0.1$  as well as the Cepheid value of  $(m - M)_0 = 23.49 \pm 0.08$  (Gallart et al. 1996c).

### 3.2. Distance from the red clump magnitude

In the past few years, there has been interest in the possible use of the red clump as a distance indicator. Using parallaxes from the *Hipparcos* catalog for nearby Galactic red clump stars, Paczyński & Stanek (1998) determined the absolute magnitude of the red clump in the solar neighborhood to be  $M_I = -0.23 \pm 0.03$ . This calibration was then used to determine the distance to the Galactic bulge (Paczyński & Stanek 1998), M31 (Stanek & Garnavich 1998) and the Magellanic Clouds (Udalski et al. 1998; Stanek et al. 1998). In the case of M31, the red clump distance agreed to within the uncertainties with the Cepheid distance while the red clump distance moduli for the Magellanic Clouds were found to be  $\sim 0.5$  mag smaller. Cole (1998) argued that  $\approx 0.3$  mag of this difference is due to the different age and metallicity distribution of red clump stars in the Magellanic Clouds as compared to those in the solar vicinity. From observations of the red clump magnitude in a sample of Galactic open clusters with metallicities in the range  $-0.4 \lesssim [Fe/H] \lesssim 0.2$  and ages

between  $\sim 2$  and  $\sim 9$  Gyr, Sarajedini (1999) found that the variation in red clump magnitude with metallicity and age largely agreed with that expected from the Bertelli et al. (1994) isochrones. Girardi & Salaris (2001) investigated in more detail the theoretical dependence of the red clump absolute magnitude on age and metallicity using the Girardi et al. (2000) isochrones and stressed the need to account for this dependence when attempting to use the red clump as a distance indicator. Furthermore, their models confirmed that red clump distance moduli to the Magellanic Clouds should be  $\sim 0.2 - 0.3$  mag larger once these population effects are included.

I have estimated the distance to NGC 6822 based upon the apparent magnitude of the red clump in conjunction with the theoretical results of Girardi & Salaris (2001). In Figure 4 the  $I$ -band magnitude distribution in the vicinity of the red clump for each field is shown for stars with  $0.5 < (V - I)_0 < 1.1$ , where each of the distributions has been corrected for extinction using the  $A_V$  values from the SFH solutions listed in Table 4. Following Paczyński & Stanek (1998), I have fit each of the distributions in Figure 4 with a function that is the sum of a 2nd order polynomial and a Gaussian. This function is given by

$$n(I_0) = a + b(I_0 - I_{0,m}) + c(I_0 - I_{0,m})^2 + \frac{N_{RC,I}}{\sigma_{RC,I}\sqrt{2\pi}} \exp\left[\frac{-(I_0 - I_{0,m})^2}{2\sigma_{RC,I}^2}\right] \quad (5)$$

where  $I_{0,m}$  represents the magnitude where the red clump peaks. An analogous function was fit also to the  $V$ -band magnitude distribution in the region of the red clump except that the quadratic term was set to zero. The results of the fits for both  $V$  and  $I$  are listed in Table 3. The average values of the red clump magnitude among the four fields are  $V_{0,m} = 23.61$  and  $I_{0,m} = 22.80$ .

In order to derive distances from these apparent magnitudes, it is necessary to assume a value for the absolute magnitude of the red clump. Girardi & Salaris (2001) give tables listing the variation of the red clump magnitude with age and metallicity for stars formed in an instantaneous star formation burst. As explained in detail in Girardi & Salaris (2001), these tables can be used to predict the absolute magnitude of the red clump for any arbitrary SFH. In order to understand the uncertainties due to the unknown metallicities of the clump stars, I have calculated the absolute magnitude of the red clump assuming a constant metallicity with two different values of  $[\text{Fe}/\text{H}]$ , namely  $[\text{Fe}/\text{H}] = -0.7$  and  $[\text{Fe}/\text{H}] = -1.7$ . The higher metallicity is similar to the highest values for the current metallicity of NGC 6822 (Pagel et al. 1980; Skillman et al. 1989) while the lower value is the lowest metallicity included in the Girardi & Salaris (2001) calculations. Using their tables in conjunction with equation (6) of their paper, I have calculated red clump  $V$  and  $I$ -band absolute magnitudes for each of the fields. In each field, I assume the SFR(t) from the results of the CMD-fitting plotted in Figure 10. Since the SFR results themselves depend upon the distance to NGC 6822, this reasoning is somewhat circular. However, the shape of the SFHs is not strongly dependent on the distance and using simply a constant SFR(t) would yield similar results for the red clump absolute magnitude. The resulting average values for  $M_I$  over the four fields are  $M_I = -0.44$  and  $M_I = -0.64$  for the high and low metallicity cases, respectively. Similarly, I obtain values of  $M_V = +0.44$  and  $M_V = -0.08$  for the high and low metallicity cases, respectively.

Applying these values to the average of the red clump magnitudes listed in Table 3, I find distance moduli of  $(m - M)_0 = 23.36 \pm 0.18$  for the  $V$ -band and  $(m - M)_0 = 23.34 \pm 0.10$  for the  $I$ -band. The values of  $(m - M)_0$  were calculated by averaging the red clump absolute magnitudes for the high and low metallicity cases while the uncertainty is simply one-half the difference. While slightly lower than the TRGB and Cepheid distance moduli determined by Gallart et al. (1996c) and in §3.1 of this paper, the values for the red clump distance agree to within the uncertainties with the other determinations.

### 3.3. Star formation history analysis

The analysis of the star formation histories in the four fields presented here relies upon the methods developed by Dolphin (1997, 2002) which I have implemented in a set of IDL routines. The analysis is nearly the same as in Wyder (2001) and thus only the differences with that paper will be emphasized here.

First a set of stellar evolutionary isochrones must be selected to generate the model Hess diagrams. I rely upon the same set of isochrones as in Wyder (2001). This primarily consists of the isochrones presented in Girardi et al. (2000) which describe the evolution of stars with masses from 0.15 to  $7 M_\odot$  for metallicities ranging from  $Z = 0.0004$  to  $Z = 0.03$ . The  $Z = 0.0001$  isochrones from Girardi et al. (1996) were added to extend the models to lower metallicities while stars more massive than  $7 M_\odot$  were included using the older Bertelli et al. (1994) isochrones. A set of files containing the combined set of isochrones was kindly provided by Andrew Dolphin.

The CMD analysis methods of Dolphin (1997, 2002) fit the observed data in the form of a binned CMD, or Hess diagram. A series of time bins are also chosen for the SFH solution. Assuming a distance, extinction, metal enrichment history and initial mass function (IMF), a Hess diagram is calculated for each time bin assuming a constant SFR within that time bin and none at other times. The errors and completeness in the photometry are included in the models using the results of the artificial star tests. The linear combination of these “basis” CMDs that best reproduces the observations determines the SFR(t). The model and observed diagrams are compared using a fit parameter derived from the Poisson distribution that is the Poisson equivalent of the  $\chi^2$  parameter derived from the Gaussian distribution. Starting from the Poisson distribution, Dolphin (2002) derived the following expression for the fit parameter:

$$\Upsilon = 2 \sum m_i - n_i + n_i \ln \frac{n_i}{m_i} \quad (6)$$

where  $m_i$  is the number of model stars in the  $i$ th bin of the model Hess diagram and  $n_i$  is the number of observed stars in the same bin. The SFH which minimizes the value of  $\Upsilon$  is the SFH which best reproduces the observations (Dolphin 2002). The average and variance of  $\Upsilon$  in each bin is one and two, respectively. The average and variance of  $\Upsilon$  summed over the entire Hess diagram depends upon the number of observed stars as well as the number of Hess diagram bins contributing to the solution (Dolphin 2002).

In the equation for the fit parameter  $\Upsilon$  in Dolphin (2002), a term is included in the models to account for the number of foreground Galactic stars. Ratnatunga & Bahcall (1985) have predicted the number counts of Galactic stars in the direction of several Local Group galaxies, including NGC 6822. According to their results, a total of 270 Galactic stars with  $17 < V < 27$  are predicted to lie within each WFPC2 field-of-view of which  $\approx 80\%$  have colors  $(B - V) > 1.3$ . This level of contamination is small compared to the  $> 10^4$  stars present in each of the CMDs and thus the foreground contamination has been neglected in all of the model Hess diagrams.

All of the SFH solutions presented in this paper were fit using 0.1 mag wide bins in  $V$  and 0.05 mag wide bins in  $(V - I)$ . A set of nine time bins were also chosen for the SFH solution that span ages from 0.01 to 15 Gyr ago.

One of the most important ingredients used in calculating the model Hess diagrams is the metal enrichment history. For the oldest stars, some measurements of their metallicities are beginning to be made. Cohen & Blakeslee (1998) measured a metallicity of  $[\text{Fe}/\text{H}] = -1.95 \pm 0.15$  and age of  $11_{-3}^{+4}$  Gyr for the star cluster Hubble VII based upon its integrated spectrum. For the field stars, Tolstoy et al. (2001) measured metallicities for 23 red giant branch stars based upon the equivalent widths of the Ca II triplet near 8500 Å. Their distribution peaks at  $[\text{Fe}/\text{H}] \approx -1.0$  with a tail of stars reaching  $[\text{Fe}/\text{H}] \approx -2.0$ .

The current metallicity in NGC 6822 has been determined both from spectra of its H II regions as well as from spectra of individual massive stars. For the H II regions, Pagel et al. (1980) and Skillman et al. (1989) measured an oxygen abundance of  $12 + \log(O/H) = 8.25 \pm 0.07$ , corresponding to  $[\text{Fe}/\text{H}] = -0.7$  for a solar O/Fe ratio. For a sample of six H II regions within NGC 6822, Chandar et al. (2000) measured a value of  $12 + \log(O/H) = 7.91 \pm 0.06$  ( $[\text{Fe}/\text{H}] = -1.0$ ).

The precise form of the age-metallicity relation in NGC 6822 is unknown. In fact, in the presence of significant outflows or inflows of gas, the metallicity may not necessarily increase monotonically with time. However, the sparse evidence summarized above indicates that the current metallicity of the gas in NGC 6822 is larger than that measured for the oldest star cluster Hubble VII although there is little observational constraints at intermediate ages.

In principle with very good, deep photometry, it is possible to simultaneously determine the  $\text{SFR}(t)$  and the metal enrichment history from the Hess diagram fits. However, there are significant degeneracies between age and metallicity in the shape and placement of the red clump and red giant branch in the theoretical isochrones and removing these degeneracies in the fits would require photometry reaching the lower main sequence, a level well below the limits of the data analyzed here.

In the absence of more precise information, a metal enrichment history was assumed in all of the models that is broadly consistent with the above observational constraints. The metallicity of the stars was assumed to increase linearly from  $Z = 0.00024$  ( $[\text{Fe}/\text{H}] = -1.9$ ) to  $Z = 0.0019$  ( $[\text{Fe}/\text{H}] = -1.0$ ) from 15 Gyr ago to the present. While there is no spread in metallicity allowed, the metallicity is assumed to increase smoothly within each time bin and thus not all of the stars



within each time bin have the same metallicity. This metal enrichment law was held constant for all of the solutions described below. The effects of varying the initial and final metallicities as well as the enrichment law are described in Wyder (2001). As in Wyder (2001), the isochrones are populated with stars assuming a power-law initial mass function with exponent  $-1.35$  that extends from  $0.1$  to  $120 M_{\odot}$ .

The extinction  $A_V$  was assumed to be constant for all the stars within each field and the corresponding reddening was calculated from the Galactic reddening law of O’Donnell (1994) with  $R_V = A_V/E(B - V) = 3.1$ . In Wyder (2001) the extinction was allowed to vary while keeping the distance constant whereas here both the extinction and distance were varied.

For each field, a set of solutions was generated for various combinations of extinction and distance. First, a coarse run was completed with step sizes of  $0.1$  mag in  $A_V$  and  $(m - M)_0$ . Then I ran a second set of solutions for each field with smaller step sizes of  $0.05$  mag in  $(m - M)_0$  and  $0.02$  mag in  $A_V$  with the range of values restricted to be within  $\pm 0.2$  mag of the minimum found in the coarse runs. The combination of  $A_V$  and  $(m - M)_0$  with the smallest value of  $\Upsilon$  is then assumed to be the best-fit solution.

Estimating the uncertainties in both the fitted parameters (i.e.  $A_V$  and  $(m - M)_0$ ) and the SFRs, is difficult in this case mainly because none of the solutions provide an acceptable fit to the data in an absolute sense. According to the discussion in Dolphin (2002), the ideal way to estimate the uncertainty is to determine the average and variance of  $\Upsilon$  from the model itself by assuming that the number of stars in each model bin follows the Poisson distribution. Then the uncertainties in all of the SFH parameters can be estimated by looking at the distribution of parameters for all solutions with values of  $\Upsilon$  with corresponding probabilities greater than some specified value. Since all of the solutions presented here are fairly far away from the true best-fit value of  $\Upsilon$ , this ideal procedure does not apply.

An alternative method of estimating the uncertainties in the values of  $A_V$ ,  $(m - M)_0$  and SFR is to construct bootstrap samples from the data (e.g. Olsen 1999). For each field, I generated 25 bootstrap versions of the photometry list by randomly choosing stars from the observed list with replacement. Then the minimum of  $\Upsilon$  was found for each bootstrap sample using exactly the same procedure as for the original data. The standard deviations of  $A_V$ ,  $(m - M)_0$  and the SFR in each bin among the solutions for the bootstrap samples are used in the next section to estimate the statistical uncertainties in the fitted parameters.

## 4. Results and Discussion

In this section the results of the SFH solutions described in the previous section are presented.

#### 4.1. Comparison of model and observed Hess diagrams

In Figures 5–8, the best-fit model Hess diagrams are compared with the observed diagrams. In each of the figures, the observed and best-fit model Hess diagrams are shown in panels (a) and (b), respectively. Panel (c) shows the difference between the observed and model diagrams divided by the expected uncertainty in the model diagram which is assumed to be given by the square root of the number of model stars in each Hess diagram bin. The latter diagram is scaled from  $-5$  (white) to  $+5$  (black). Finally, a map of the contribution to the overall  $\Upsilon$  sum in equation (6) is shown in panel (d).

Overall, the model Hess diagrams contain the major features that are in the observed diagrams and reproduce their relative strengths. However, it is clear from Figures 5–8 that the models and observations do differ in detail. Except for the outermost C1 field, the plume of blue main sequence stars is wider in the observations than in the models. Since the effects of errors in the photometry are included in the models using the artificial star test results, the observed width is not due to errors alone. One explanation for the difference is that each of the model diagrams assumes a single value for the extinction and reddening within each field. If a range of reddenings were allowed in the models within each of the fields, then the main sequence would widen.

In most of the fields, the models do not reproduce the observed stars at the red edge of the red giant branch. The shape of the red clump is different as well between the models and data. Since the colors of the red giant branch stars and the red clump morphology are strongly affected by metallicity, this difference could indicate that the age-metallicity relation I have adopted is incorrect. On the other hand, the red clump tilts up and to the left in the observed Hess diagrams, particularly in the C12 and C18 fields, and is oriented roughly parallel to the reddening vector. Hence, a range of reddenings within each field might also account for part of the differences between the observations and models.

Finally, it is important to note that there are significant uncertainties in the stellar evolutionary models which may account for some of the differences between the model and observed Hess diagrams. For example, Gallart et al. (2003) compared the Padova isochrones (Girardi et al. 2000) in the 1 – 3 Gyr age range with those from Yi et al. (2001) and found significant differences in the shapes of the RGB, subgiant branch and main sequence turn-off. These differences were attributed to different assumptions made regarding the input physics such as convective overshoot and the equation of state. In addition, the methods used to transform luminosities and effective temperatures into observable magnitudes and colors are different between the two isochrone sets and lead to differences in the resulting tracks in the CMD.

## 4.2. Distance

The distance moduli corresponding to the best-fit SFHs are listed in Table 4 while Table 5 gives the results of the solutions for the bootstrap samples. Columns (2) and (3) of Table 5 list the average and standard deviation, respectively, calculated from the solutions of the bootstrap samples. The average values from the bootstrap samples are similar to the best-fit values from the solutions to the original data, indicating that there is no bias inherent in the Hess diagram fitting itself. The standard deviations from the bootstrap fits have values of 0.03 – 0.06 mag and I assume these values as the statistical error in the distances due to the fitting of the observed Hess diagrams. This does not include any potential systematic errors due to the various assumptions made in construction of the model Hess diagrams. These best-fit distance moduli of 23.15-23.25 are smaller than the red clump value of  $(m - M)_0 = 23.34 \pm 0.10$  determined in §3.2 as well as the distance moduli determined by Gallart et al. (1996c) from both Cepheids and the TRGB which yielded values of  $23.49 \pm 0.08$  and  $23.4 \pm 0.1$ , respectively. The difference between the distances determined here and the Cepheid, TRGB and red clump determinations are larger than the random errors quoted in Table 5. However, there are likely systematic errors in the distances determined from the CMD-fitting due to the assumptions made about the metal enrichment as I argue below.

While the distances determined from the SFH solutions are sensitive to features in the entire CMD, the use of the Poisson fit parameter means that those bins of the Hess diagram with the largest numbers of stars will contribute most to the best-fit value of the distance. As is obvious from the CMDs in Figure 2, the red clump is the most prominent feature in all of the diagrams and its magnitude has a large influence on the derived value of the distance.

If I calculate the red clump absolute magnitudes in the same way as in §3.2 except using the same age-metallicity relation as used in the SFH solutions, I obtain values of  $M_V = +0.301$  and  $M_I = -0.517$ , leading to a distance modulus of  $(m - M)_0 = 23.31$  from both the  $V$  and  $I$  magnitudes. These values are  $\approx 0.1$  mag larger than the values determined from the fits to the full CMD listed in Table 4 despite adopting the identical age-metallicity relation and SFR(t). While the red clump is the most dominant feature in each of the CMDs and has a large influence in the best-fitting distance, it is important to note that it is the entire CMD that determines the distance. Hence, there must be other features in the CMD which are also affecting these distance determinations. Furthermore, the SFH is fit to the  $V, V - I$  CMD and thus it is the  $V$ -band absolute magnitude of the models which directly determines the distance. As has been pointed out previously (i.e. Girardi & Salaris 2001), the value of  $M_V$  for the red clump is more sensitive to age and metallicity effects than  $M_I$ .

The difference of  $\approx 0.4$  mag between the value of  $M_V$  for  $[\text{Fe}/\text{H}] = -0.7$  and  $[\text{Fe}/\text{H}] = -1.7$  is an estimate of the systematic effects of the unknown age-metallicity relation on the distance determined from the fits to the observed CMDs. Thus, the distance moduli listed in Table 4 from the SFH solutions have systematic uncertainties of  $\pm \sim 0.2$  mag due simply to metallicity effects. Averaging the results for the four fields yields a distance modulus of  $(m - M)_0 = 23.20 \pm 0.05 (\pm 0.2)$

where the first error is the statistical error from the bootstrap analysis and the error in parentheses is the systematic error due to our lack of knowledge about the chemical enrichment history.

These results underscore the caution that must be taken when attempting to determine the distance from fitting the CMD. It is important to understand the systematic effects of the assumptions made regarding the parameters used in generating the model Hess diagrams.

### 4.3. Extinction

The best-fitting values of the extinction in each field are listed in Table 4 whereas the results of the bootstrap analysis are shown in Table 5. As was the case for the distance determinations, the average values of  $A_V$  from the bootstrap samples are nearly the same as the values from the best-fit to the actual data, indicating no inherent bias in the value of  $A_V$  due to the fitting procedure alone. The standard deviations for each of the fields from the bootstrap analysis are  $\approx 0.01$  mag. Estimating any systematic errors in the extinction due to the assumptions made about the metallicities and other parameters is more difficult since the determination of the extinction is sensitive to both the color and magnitude of features in the CMD. However, one crude estimate can be made by examining the spread in the red clump magnitudes  $V_{0,m}$  listed in Table 3. Since these values have been corrected for the extinction using the values from fitting the CMD, they should yield the same number if any differences in stellar populations among the four fields are neglected. Half of the full spread of values for  $V_{0,m}$  is 0.05 mag which I will assume as the uncertainty in the extinction values listed in Table 4.

There is a trend of increasing extinction going from fields C25 to C1, or equivalently, going from east to west across the minor axis of the galaxy. While this direction also corresponds to decreasing distance from the Galactic plane, the difference of  $\approx 0.4$  mag among the four fields across only  $\approx 10'$  would be difficult to explain as variations in the Galactic foreground extinction. The extinction determined for the C25 field of  $A_V = 0.84$  is comparable to the foreground Galactic extinction to NGC 6822 of  $A_V \approx 0.7$  as determined from the Schlegel et al. (1998) reddening maps. The higher extinction values in the other three fields imply the existence of additional extinction internal to NGC 6822 itself. From observations of OB stars in NGC 6822, Massey et al. (1995) found a similar increase in the reddening from  $E(B - V) = 0.26$  ( $A_V = 0.81$ ) in the outer regions to  $E(B - V) = 0.45$  ( $A_V = 1.4$ ) in the bar. A similar trend was found for the four other *HST* fields presented in Wyder (2001) where the extinction in the bar was determined to be  $A_V \approx 1.0$  and smaller in the outer regions. The one exception to these trends is the C1 field where the best fit extinction is  $A_V = 1.2$  despite the fact that this is the field located the farthest from the bar.

The dust responsible for the extinction internal to NGC 6822 is expected to emit at far infrared wavelengths. A contour map of the  $60\mu\text{m}$  emission in NGC 6822 from Rice (1993) as measured by the IRAS satellite is shown in Figure 9 where the locations of the four *HST* fields analyzed here are indicated. As in Wyder (2001), the extinction values derived from fitting the CMD are

roughly correlated with the FIR emission. In fact the C1 field which has the largest value of the extinction is coincident with a local peak in the  $60\mu\text{m}$  emission. This FIR peak contains the H II regions  $K\alpha$ ,  $K\beta$  and HK 1 (Hodge et al. 1988) and it would be reasonable to expect that the dust responsible for the extinction in the C1 field and this peak in the FIR emission is associated with these star formation regions. In general there is a good correspondence between the locations of H II regions and OB associations in NGC 6822 and peaks in the FIR emission although there are substantial spatial variations in the ratio of FIR to  $H\alpha$  luminosity (Gallagher et al. 1991; Israel et al. 1996). The amount of FIR emission is expected to be proportional to both the amount of dust and the strength of the UV radiation field. However, star formation regions are also those areas where increased densities of gas and dust are expected. The correlation between the FIR surface brightness and the extinction inferred from the CMDs suggests that the varying FIR emission is indeed tracing the distribution of dust in NGC 6822 rather than solely being due to variations in the interstellar radiation field.

#### 4.4. Star Formation Histories

The SFRs per area averaged over the field-of-view for each of the four fields are plotted in Figure 10. The error bars in age denote the limits of the time bins chosen for the SFH solutions. The error bars in the SFRs in each time bin are computed from the fits to the 25 bootstrap samples of each CMD. These uncertainties are calculated as the standard deviations of the SFRs in each bin. It is important to emphasize that the SFRs in each of the bins are not independent since the total number of stars for any model is conserved. Therefore, a decrease in the SFR in one time bin is accompanied by an increase in the SFR in another bin.

For the older ages ( $> 1$  Gyr), the shapes of the SFHs among the four fields are similar although the overall normalization varies due to the different numbers of stars within each field. The SFRs are fairly constant or perhaps slightly increasing with time in some of the fields. For the C1, C18 and C25 fields, the SFR declines at an age of  $\sim 600$  Myr by a factor of  $\sim 2 - 4$  while for the C12 field centered on the bar, the SFR remains roughly constant four ages less than 600 Myr with an increase for the youngest time bin. Despite the drop in star formation seen in the three other fields, there are some stars present in these fields with ages as young as a few 10s of Myr old. Thus, the outer regions sampled here do not represent a pure population II halo as many larger galaxies possess.

As shown by Kennicutt (1998), the relationship between the global average SFR per area and the surface density of atomic plus molecular gas in galaxies is well represented by the following relation

$$\Sigma_{SFR} = (2.5 \pm 0.7) \times 10^{-4} \left( \frac{\Sigma_{gas}}{1 \text{ M}_{\odot} \text{pc}^{-2}} \right)^{1.4 \pm 0.15} \text{ M}_{\odot} \text{ yr}^{-1} \text{ kpc}^{-2} \quad (7)$$

This global relationship can be used to compare the SFRs determined here from the CMD-fitting with the SFRs implied by the star formation law in equation (7). Using the position angle, center

and inclination derived from the H I observations of Weldrake et al. (2002), the four *HST* fields lie at galactocentric radii of  $\sim 350 - 500''$ . At these radii, the azimuthally averaged H I surface density is  $\Sigma_{HI} \approx 4 \text{ M}_{\odot} \text{pc}^{-2}$  (Weldrake et al. 2002). Of the galaxies used in the Kennicutt (1998) sample, the H I gas accounts for one-half the total gas mass on average although there is a large dispersion in the atomic gas fraction in the sample. Assuming that one-half of the gas mass in NGC 6822 is H I, the total gas surface density at the radii sampled by the *HST* fields is  $\Sigma_{gas} \approx 8 \text{ M}_{\odot} \text{pc}^{-2}$ . According to equation (7), this corresponds to a SFR surface density of  $\Sigma_{SFR} = (4.6 \pm 1.3) \times 10^{-3} \text{ M}_{\odot} \text{yr}^{-1} \text{kpc}^{-2}$  where the uncertainty is derived from the errors in the parameters in equation (7). This SFR surface density is comparable to that observed for the average old ( $> 1 \text{ Gyr}$ ) SFRs in all the fields. This approximate agreement between the SFRs from the global SFR law and the SFRs calculated from the CMDs means that it would have been possible for the gas in NGC 6822 to be distributed many Gyr ago as it is today and be able to produce the SFRs that have been determined for the older stars. Therefore, there is no need for a large scale redistribution of gas or stars to account for the SFRs shown in Figure 10.

With the exception of the C12 field centered on the bar, the recent SFRs are smaller than the Schmidt law value. However, star formation in most galaxies tends to be quite patchy and occurs in associations of various sizes that gradually dissolve over time. In particular, the C12 field contains part of OB associations 9 and 11 from the list in Hodge (1977). The C25 field contains part of OB association 15 and the remaining two fields contain none of the associations from Hodge (1977). Nevertheless, the recent star formation is not entirely confined to the OB associations since there are bright main sequence stars in each pointing scattered across the field-of-view. Since each field samples a relatively small area, the precise values of the recent SFRs in each field are sensitive to this irregular spatial distribution of young stars. As a result, the SFR surface densities in each field may differ from the azimuthally averaged value. Furthermore, the gas density is also somewhat clumpy which would cause the local gas density to differ from the azimuthally averaged value as well.

In their ground-based data covering a much larger area of NGC 6822, Gallart et al. (1996b) found that the SFR 100 – 200 Myr ago increased by a factor of 2 in the outer regions and in the center of the bar and increased by a factor of 4 – 6 at the ends of the bar. de Blok & Walter (2000) detected a  $2.0 \times 1.4 \text{ kpc}^2$  hole in the H I gas lying to the east of the bar that would have an age of roughly 100 Myr based upon its size. One possible explanation for the increase in SFR and the creation of the H I hole  $\sim 100 \text{ Myr}$  ago is an interaction between the main body of the galaxy and the H I cloud to the NW of the bar (de Blok & Walter 2000). It would be reasonable to assume that similar variations in the SFR have occurred throughout the history of NGC 6822 due to similar relatively minor interactions. Since the resolution in age for the SFH solutions described here decreases quickly with increasing age, it would be possible for short term star formation bursts to remain undetected in the current data. However, the overall picture that can be drawn from the SFHs in Figure 10 is that NGC 6822 has been forming stars at a more or less constant rate over its lifetime with no evidence for large long term variations in the SFR. This picture is consistent with

the relatively isolated position that NGC 6822 occupies in the Local Group and the corresponding lack of major interactions that it has likely experienced.

I am grateful to Andrew Dolphin for providing me with this HSTPHOT photometry programs as well as for his generous help in assisting me to understand his star formation history analysis methods. I am also grateful to Paul Hodge for allowing me to work on this data and his encouragement and guidance. Support for proposal 8314 was provided by NASA through a grant from the Space Telescope Science Institute, which is operated by the Association of Universities for Research in Astronomy, Inc., under NASA contract NAS 5-26555.

### REFERENCES

- Bertelli, G., Bressan, A., Chiosi, C., Fagotto, F., & Nasi, E. 1994, *A&AS*, 106, 275
- Chandar, R., Bianchi, L., & Ford, H. C., 2000, *AJ*, 120, 3088
- Cohen, J. G., & Blakeslee, J. P. 1998, *AJ*, 115, 2356
- Cole, A. A. 1998, *ApJ*, 500, L137
- Da Costa, G.S., & Armandroff, T. E. 1990, *AJ*, 100, 162
- de Blok, W. J. G., & Walter, F. 2000, *ApJ*, 537, L95
- Dolphin, A. E. 1997, *New Astronomy*, 2, 397
- Dolphin, A. E. 2000, *PASP*, 112, 1383
- Dolphin, A. E. 2002, *MNRAS*, 332, 91
- Dolphin, A. E., et al. 2002, *AJ*, 123, 3154
- Gallagher, J. S., Hunter, D. A., Gillet, F. C., & Rice, W. L. 1991, *ApJ*, 371, 142
- Gallart, C., Aparicio, A., Bertelli, G., & Chiosi, C. 1996a, *AJ*, 112, 1950
- Gallart, C., Aparicio, A., Bertelli, G., & Chiosi, C. 1996a, *AJ*, 112, 2596
- Gallart, C., Aparicio, A., & Vílchez, J. M. 1996c, *AJ*, 112, 1928
- Gallart, C., et al. 2003, *AJ*, 125, 742
- Girardi, L., Bressan, A., Bertelli, G., & Chiosi, C. 2000, *A&AS*, 141, 371
- Girardi, L., Bressan, A., Chiosi, C., Bertelli, G., & Nasi, E. 1996, *A&AS*, 117, 113
- Girardi, L., & Salaris, M. 2001, *MNRAS*, 323, 109

- Hodge, P. W. 1977, *ApJS*, 33, 69
- Hodge, P. W. 1980, *ApJ*, 241, 125
- Hodge, P. W., Kennicutt, R. C., & Lee, M. G. 1988, *PASP*, 100, 917
- Hodge, P. W., Smith, T., Eskridge, P., MacGillivray, H., & Beard, S. 1991, *ApJ*, 379, 621
- Israel, F. P., Bontekoe, Tj. R., & Kester, D. J. M. 1996, *A&A*, 308, 723
- Kennicutt, R. C. 1998, *ApJ*, 498, 541
- Komiyama, Y. 2002, *The Outer Edges of Dwarf Irregular Galaxies*, 2002 Lowell Workshop On-Line Proceedings, <http://www.lowell.edu/Workshop/Lowell02/Proceedings>
- Lee, M. G., Freedman, W. L., & Madore, B. F. 1993, *ApJ*, 417, 553
- Martínez-Delgado, D., Gallart, C., & Aparicio, A. 1999, *AJ*, 118, 862
- Minniti, D. & Zijlstra, A. A. 1997, *AJ*, 114, 147
- O'Donnell, J. E. 1994, *ApJ*, 422, 158
- Olsen, K. A. G. 1999, *AJ*, 117, 2244
- Massey, P., Armandroff, T. E., Pyke, R., Patel, K., & Wilson, C. D. 1995, *AJ*, 110, 2715
- Paczyński, B., & Stanek, K. Z. 1998, *ApJ*, 494, L219
- Pagel, B. E. J., Edmunds, M. G., & Smith, G. 1980, *MNRAS*, 193, 219
- Ratnatunga, K. U., & Bahcall, J. N. 1985, *ApJS*, 59, 63
- Rice, W. 1993, *AJ*, 105, 67
- Sarajedini, A. 1999, *AJ*, 118, 2321
- Seth, A., & Hodge, P. W. 2003, in preparation
- Schlegel, D. J., Finkbeiner, D. P., & Davis, M. 1998, *ApJ*, 500, 525
- Skillman, E. D., Terlevich, R., & Melnick, J. 1989, *MNRAS*, 240, 563
- Stanek, K. Z., & Garnavich, P. M. 1998, *ApJ*, 503, L131
- Stanek, K. Z., Zaritsky, D., & Harris, J. 1998, *ApJ*, 500, L141
- Tolstoy, E., Irwin, M. J., Cole, A. A., Pasquini, L., Gilmozzi, R. 2001, *MNRAS*, 327, 918
- Udalski, A., Szymański, M., Kubiak, M., Pietrzyński, Woźniak, P., & Żebruń, K. 1998, *Acta. Astron.*, 48, 1



Weldrake, D., de Blok, E., & Walter, F. 2002, MNRAS, in press

Wyder, T. K. 2001, AJ, 122, 2490

Yi, S., Demarque, P., Kim, Y.-C., Lee, Y.-W., Ree, C. H., Lejeune, T., & Barnes, S. 2001, ApJS, 136, 417

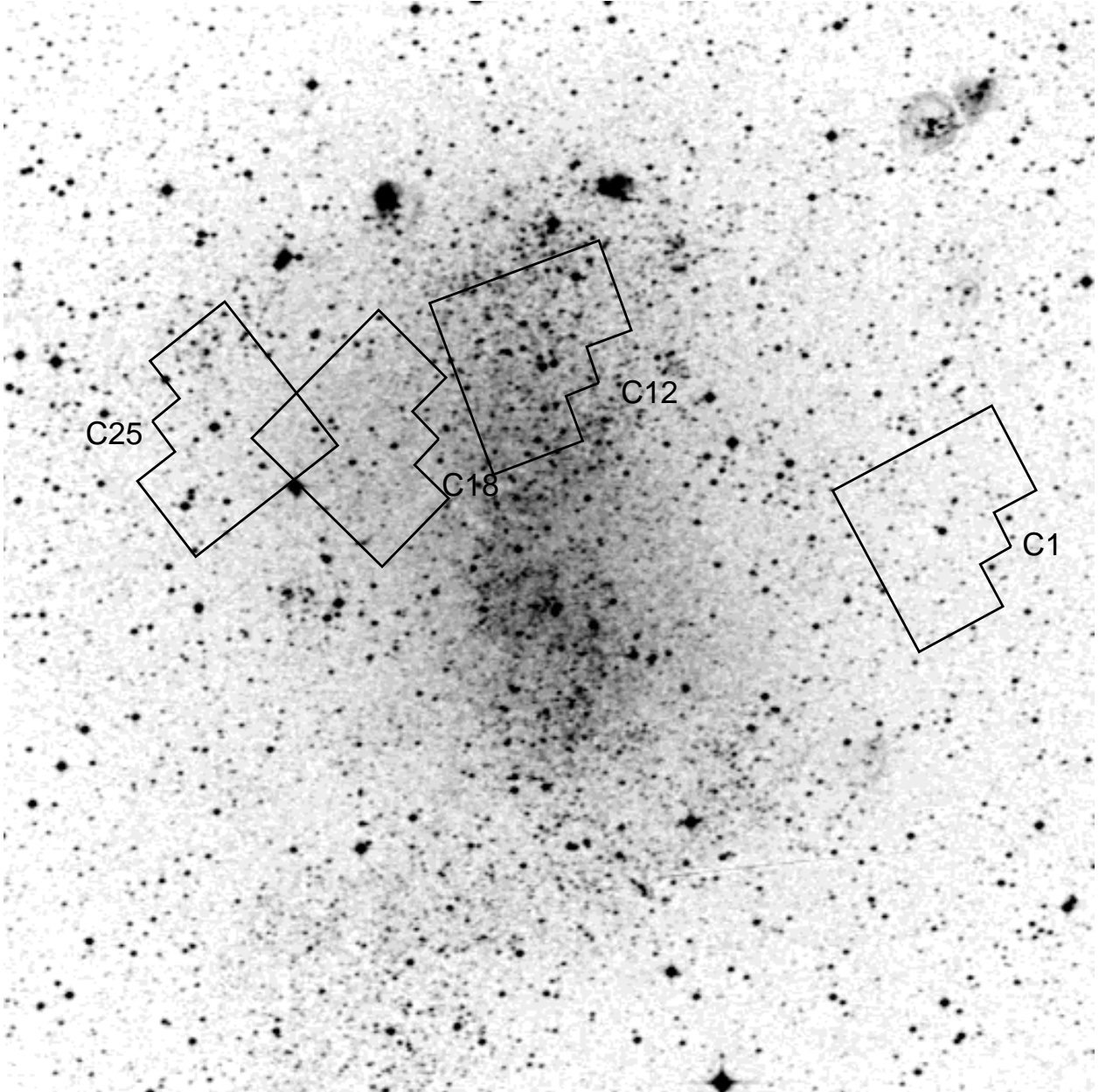


Fig. 1.— Digitized Sky Survey image of NGC 6822 (North up, East to the left). The field-of-view is  $15'$ , or about the same size the galaxy's  $D_{25}$  diameter. The positions of the four WFPC2 fields analyzed here are shown. Each is labeled by the star cluster from the list in Hodge (1977) that is centered on the PC chip.

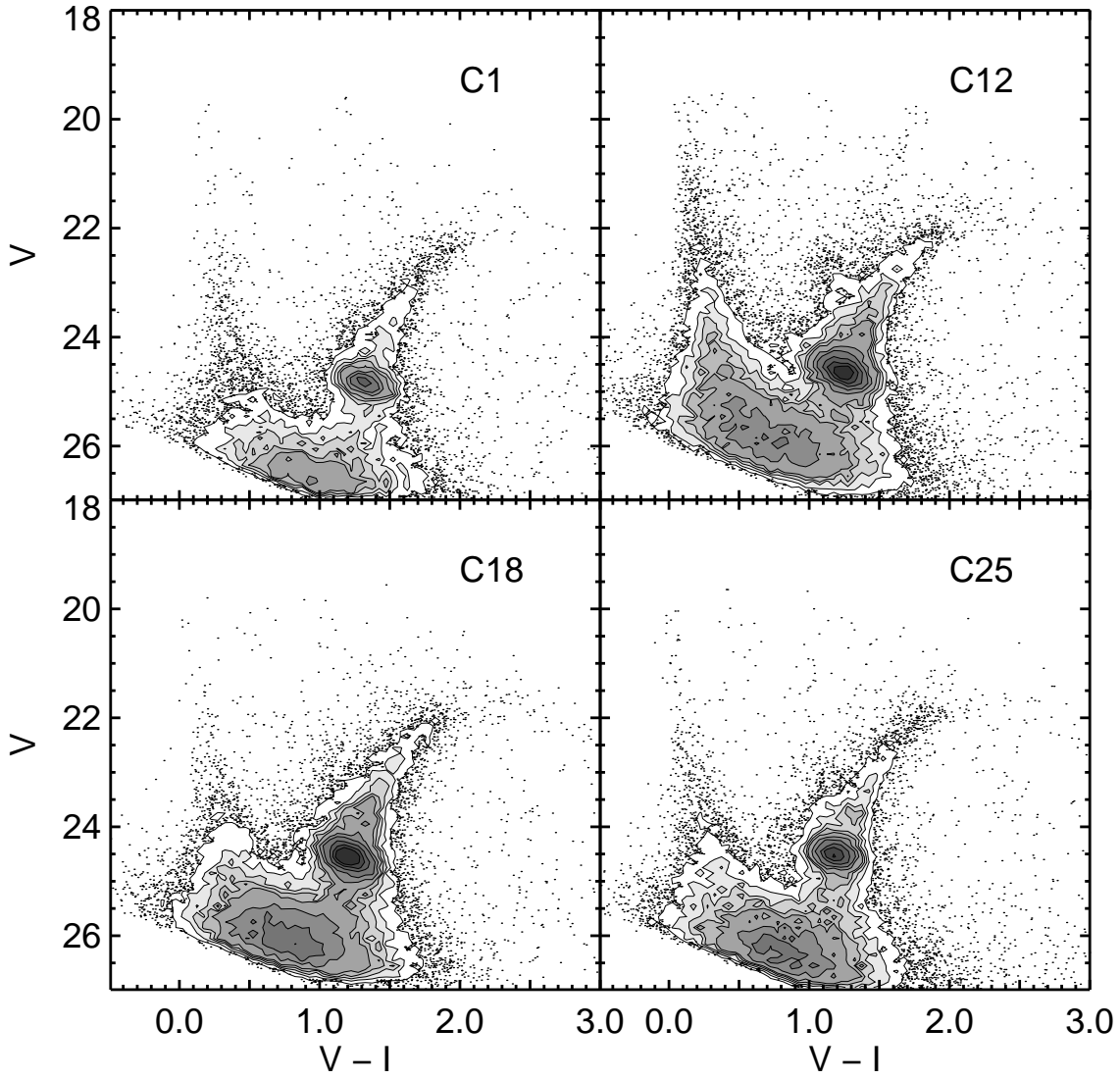


Fig. 2.— Observed  $VI$  CMDs for all stars detected in the WF chips of each field. The contour levels correspond to stellar densities of 20, 40, 60, 80, 100, 150, 200, 300, 400 and 500 stars  $\text{decimag}^{-2}$ . For those areas of each diagram with a density of stars smaller than the lowest contour, each individual star is plotted.

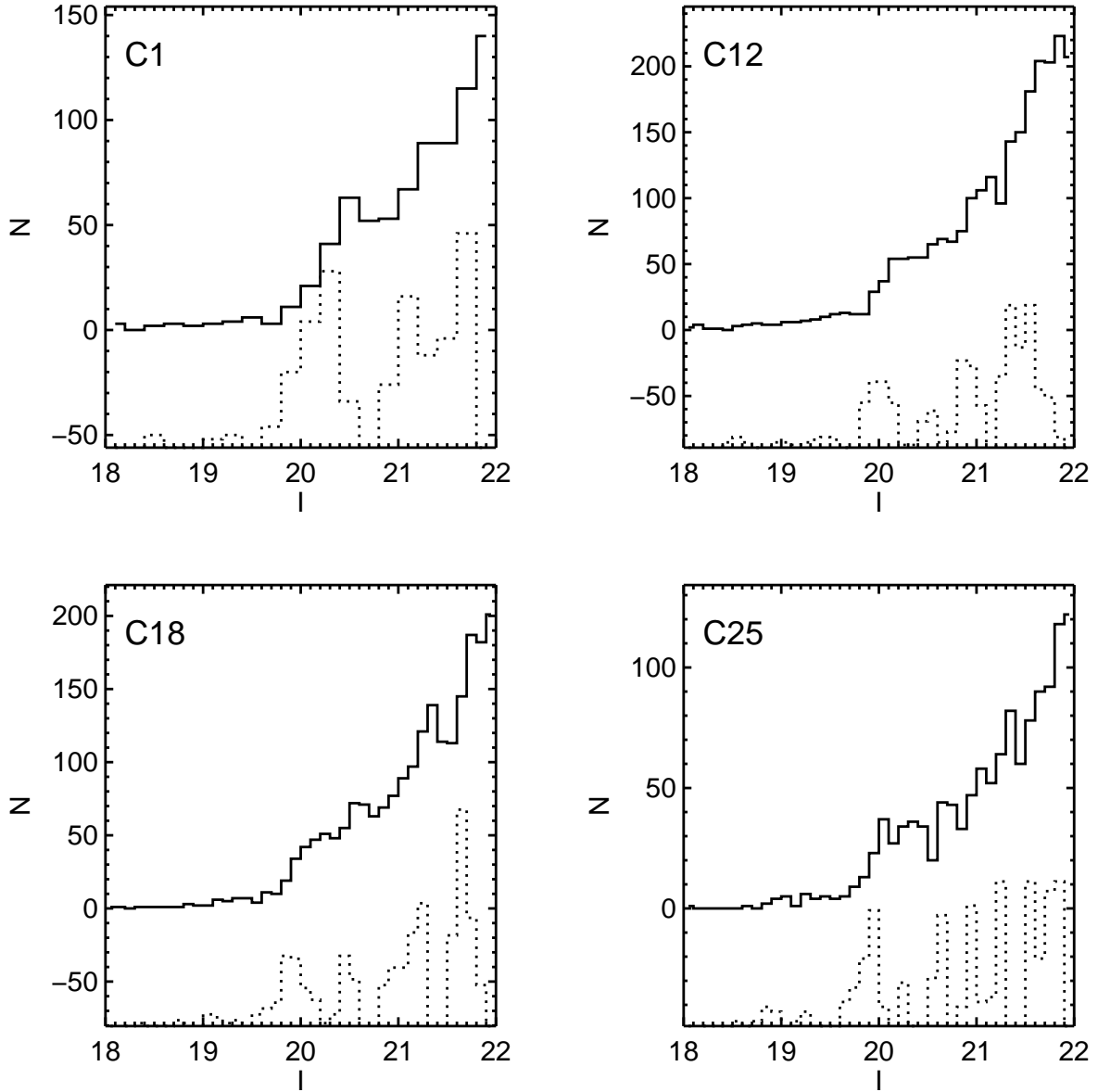


Fig. 3.—  $I$ -band RGB magnitude distribution for each of the fields. In each panel the magnitude distribution for stars with  $1.0 < V - I < 2.2$  is plotted as the solid line. The dotted line is the magnitude distribution convolved with an edge-detecting Sobel kernel  $(-2, 0, 2)$  and has been offset for clarity by an arbitrary amount in each panel. No correction for extinction has been applied.

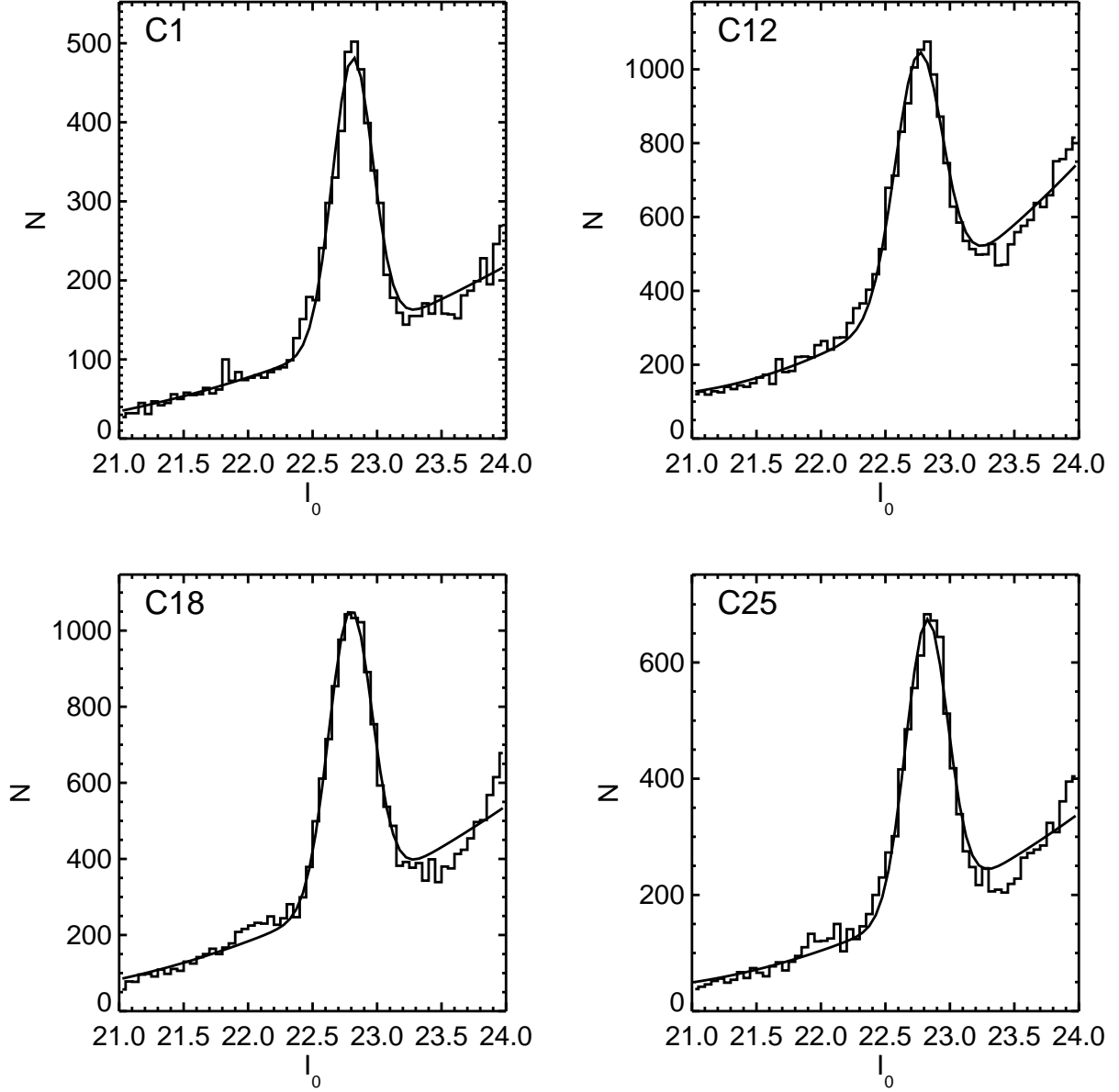


Fig. 4.—  $I$ -band magnitude distribution for each field in the region of the red clump. Each panel plots the magnitude distribution for stars with  $0.5 < (V - I)_0 < 1.5$  as a histogram. The smooth curve in each panel is the best-fit Gaussian plus quadratic to the data. In each field, the data were corrected for extinction using the values determined from the CMD-fitting, as described in the text.

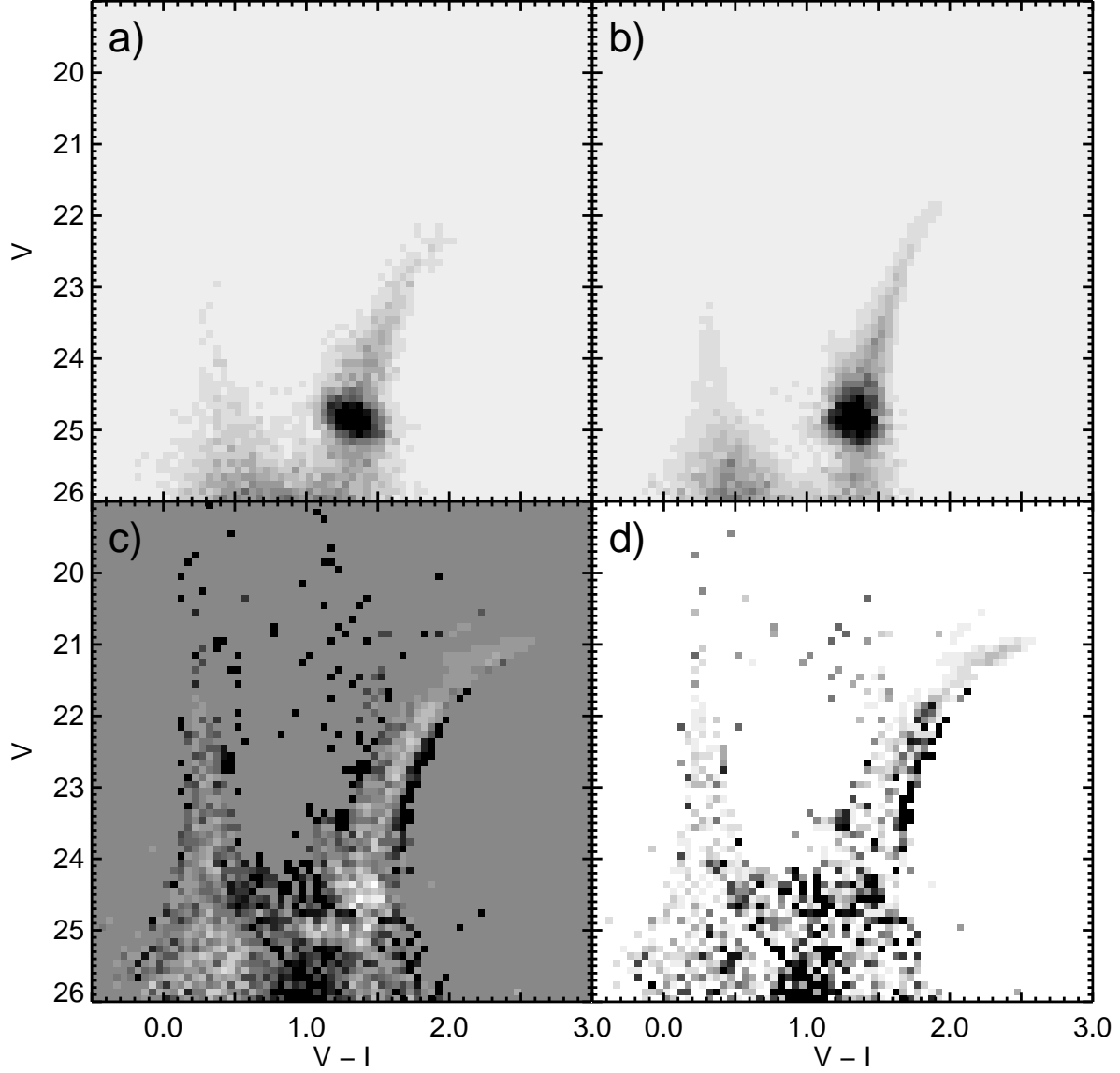


Fig. 5.— Comparison of the observed and model Hess diagrams for the C1 field. Panels (a) and (b) show the observed and best-fit model Hess diagrams, respectively. Panel (c) shows the difference between the observed and model diagrams divided by the uncertainty in the model diagram. The data in this panel are plotted from  $-5$  (white) to  $+5$  (black) and thus the black areas are where there are more observed than model stars. Panel (d) plots the contribution of each Hess diagram bin to the overall value of  $\Upsilon$  as defined in equation (6).

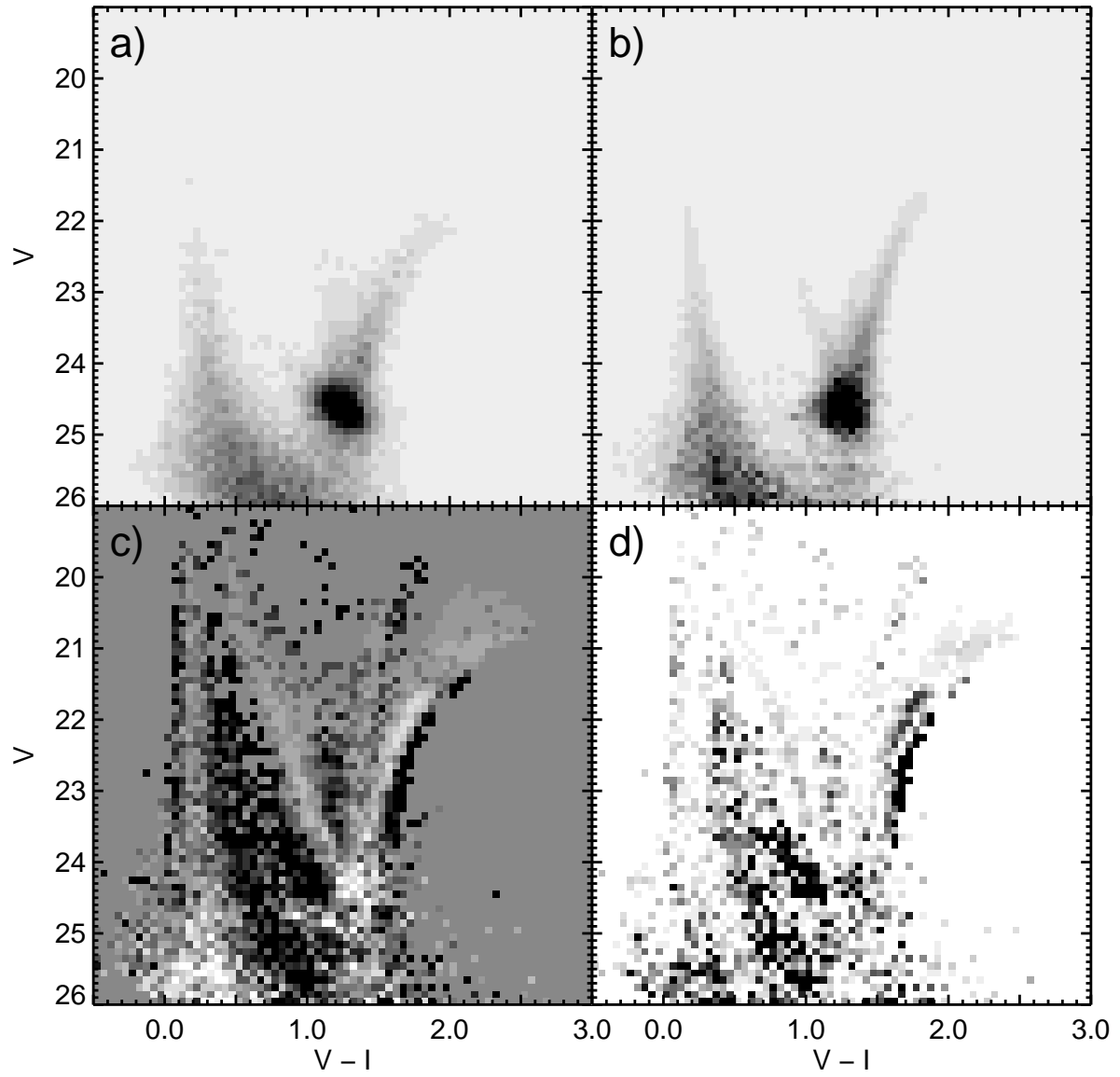


Fig. 6.— Same as Figure 5, except for the C12 field.

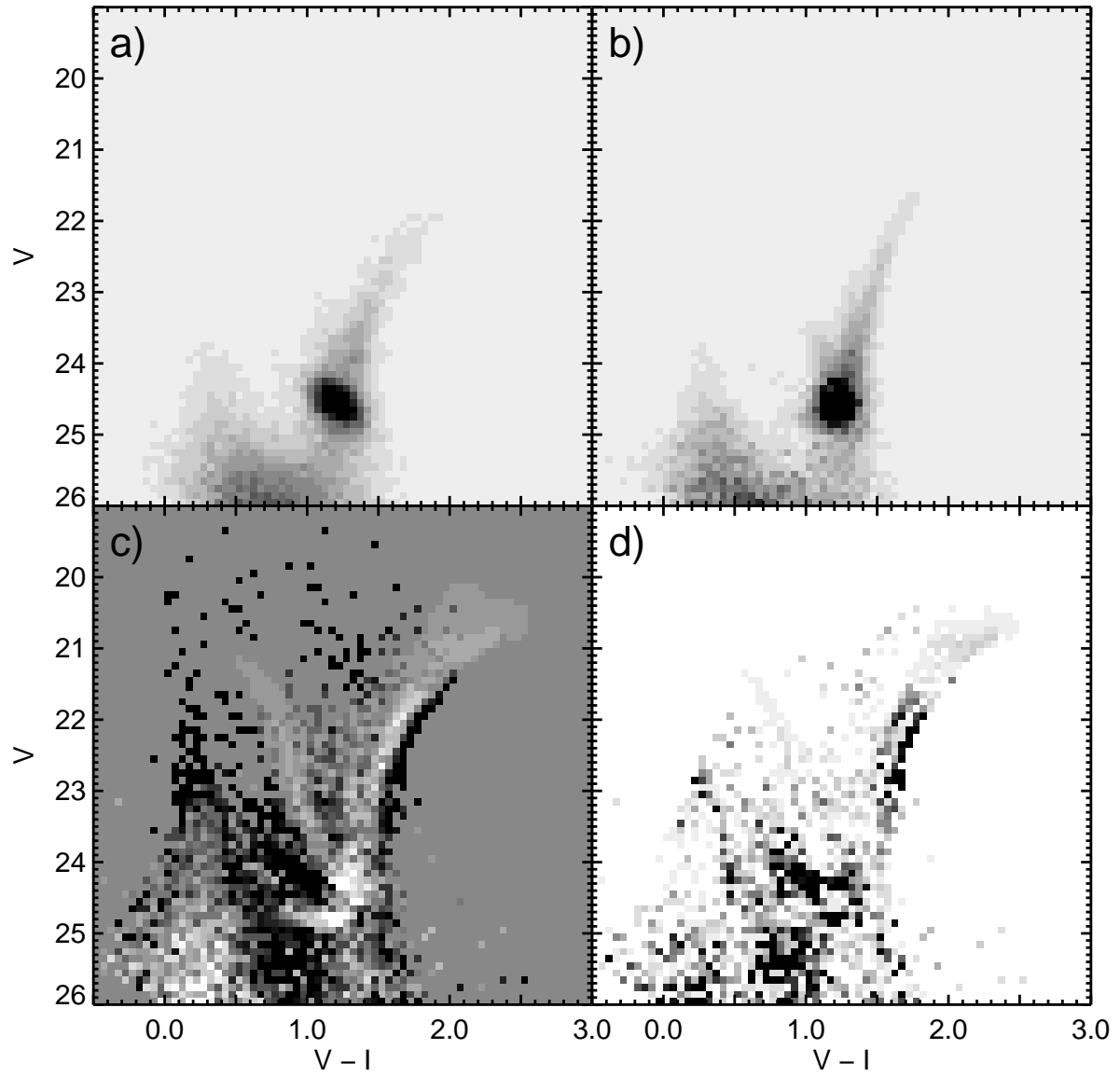


Fig. 7.— Same as Figure 5, except for the C18 field.



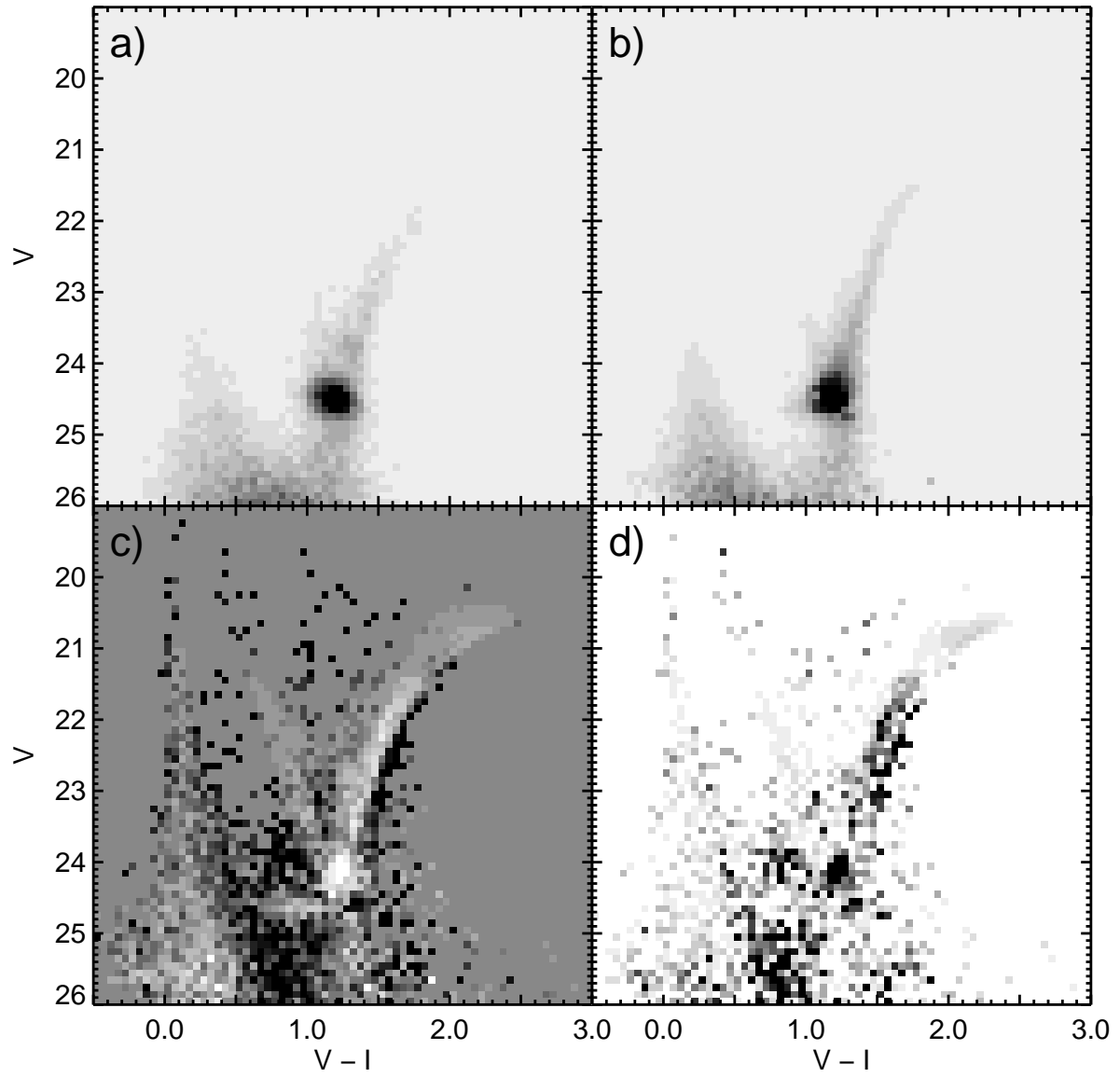


Fig. 8.— Same as Figure 5, except for the C25 field.

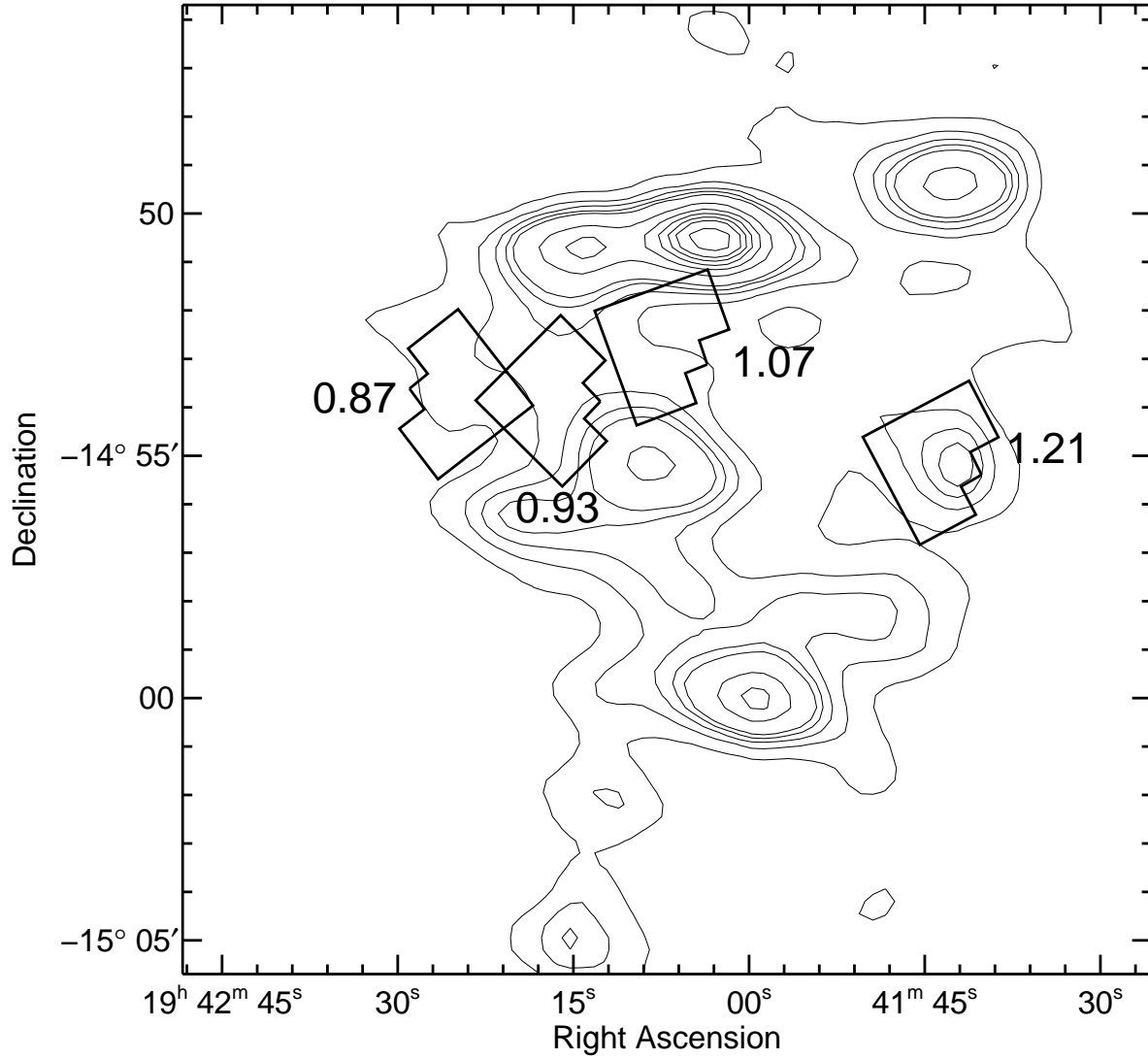


Fig. 9.— Location of the four WFC2 fields overlaid on the  $60\mu\text{m}$  emission measured by the IRAS satellite (Rice 1993). The coordinates are epoch 1950 and the value of the extinction  $A_V$  determined from the CMD fitting is shown next to each field. The contour levels corresponding to surface brightnesses of 1, 2, 3, 4, 5, 10, 15, 20, 25, 30 and  $40 \text{ MJy sr}^{-1}$ .

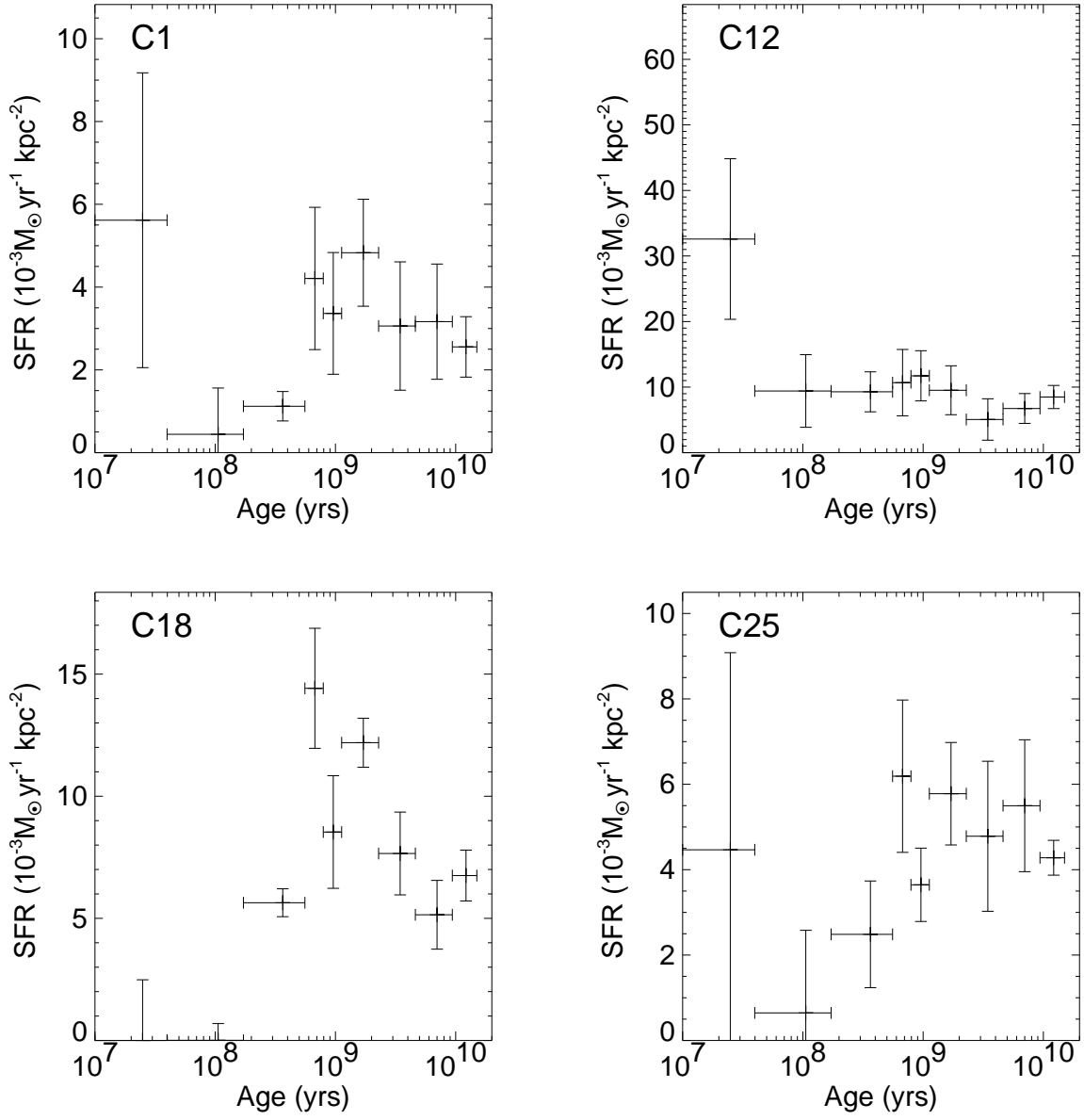


Fig. 10.— The star formation rate per area as a function of age from the present for all four pointings in NGC 6822.

Table 1. Summary of observations

Field	Dataset	Filter	Exp. time (sec)	Date of obs.
C1	u5ch0103r	F555W	800	2000 Jun 3
	u5ch0104r	F555W	400	2000 Jun 3
	u5ch0105r	F814W	600	2000 Jun 3
	u5ch0106r	F814W	600	2000 Jun 3
C12	u5ch0203r	F555W	800	2000 Jun 3
	u5ch0204r	F555W	400	2000 Jun 4
	u5ch0205r	F814W	600	2000 Jun 4
	u5ch0206r	F814W	600	2000 Jun 4
C18	u5ch0303r	F555W	800	2000 Jun 4
	u5ch0304r	F555W	400	2000 Jun 4
	u5ch0305r	F814W	600	2000 Jun 4
	u5ch0306r	F814W	600	2000 Jun 4
C25	u5ch0403r	F555W	800	1999 Sep 24
	u5ch0404r	F555W	400	1999 Sep 24
	u5ch0405r	F814W	600	1999 Sep 24
	u5ch0406r	F814W	600	1999 Sep 24

Table 2. Tip of the red giant branch distance to NGC 6822

Field	$I_{TRGB}$	$(V - I)_{-3.5}$	$(V - I)_{TRGB}$	$(m - M)_0$
C1	$20.30 \pm 0.30$	1.77	1.94	$23.56 \pm 0.30$
C12	$20.00 \pm 0.10$	1.77	1.90	$23.38 \pm 0.10$
C18	$19.90 \pm 0.10$	1.75	1.88	$23.36 \pm 0.10$
C25	$19.95 \pm 0.15$	1.71	1.87	$23.47 \pm 0.15$

Table 3. Gaussian fits to the red clump magnitude distribution

Field	$N_{RC,V}$	$V_{0,m}$	$\sigma_{RC,V}$	$N_{RC,I}$	$I_{0,m}$	$\sigma_{RC,I}$
C1	122	23.63	0.16	140	22.81	0.16
C12	273	23.56	0.19	306	22.76	0.18
C18	258	23.60	0.17	318	22.79	0.17
C25	178	23.66	0.15	201	22.82	0.16

Table 4. Best fit values of  $A_V$  and  $(m - M)_0$

Field	$(m - M)_0$	$A_V$
C1	23.20	1.20
C12	23.15	1.06
C18	23.25	0.94
C25	23.20	0.84

Table 5. Results of bootstrap solutions

Field	$\langle(m - M)_0\rangle$	$\sigma(m - M)_0$	$\langle A_V\rangle$	$\sigma(A_V)$
C1	23.208	0.059	1.208	0.017
C12	23.150	0.050	1.065	0.010
C18	23.238	0.033	0.950	0.010
C25	23.232	0.045	0.839	0.011